Heliyon

Expounding structures of roller compacted concrete dam specimens by means of hard conventional X-ray inspection

W. C. Godoi [a],*, G. Coraiola [a], S. Ribeiro Junior [c], V. Swinka-Filho [b,c], K. de Geus [c,d], K. Franke Portella [b], B. L. Medeiros [b], F. Cunha de Andrade [d], M. G. Hönnicke [e]

[a] Universidade Tecnológica Federal do Paraná, 80230-901, Curitiba, PR, Brazil

[b] Lactec, Caixa Postal 19067, 81531-990, Curitiba, PR, Brazil

[c] Universidade Federal do Paraná, 81531-980, Curitiba, PR, Brazil

[d] Copel Geração e Transmissão S. A., 81200-240, Curitiba, PR, Brazil

[e] Universidade Federal da Int. Lat.-Americana, Foz do Iguacu, PR 85867-990, Brazil

* Corresponding author.

E-mail address: walmorgodoi@utfpr.edu.br (W.C. Godoi).

Abstract

A simple solution to improve the contrast between the different concrete composites in X-ray imaging (radiography and tomography) of a highly compressed composite sample of real size roller compacted concrete (RCC) specimens is presented. This is made by applying a 9.5 mm thick Copper (Cu) filter at the output window of the X ray tube in a conventional X-ray inspection equipment. Our results show that with the employed filtration, at 140 kV and 200 kV, we were able to distinguish the gravel from the other concrete composites even in a highly compacted specimen. Cement and sand grains as well as porosity were not detected mainly due to the low spatial resolution of our detector system. This suggests a further improvement by using the now available high voltage microfocus X-ray tube ($>= 200$ kV), a bow-tie (or through) Cu filters and a high resolution flat panel detector for phase contrast imaging on real size compacted concrete specimens.

Keywords: Civil engineering, Structural engineering

1. Introduction

The properties of concrete are directly influenced by internal defects, whether inclusions or voids, resulting from the manufacturing process or degradation by percolation leaching, dissolution and parallel chemical reactions [1]. On the other hand, another factor which plays an important role in the durability of the cement based composites is the porosity. It can be classified in gel voids, capillary voids and macro voids [2].

Performance evaluation of concrete structures is carried out usually through destructive methods, such as mechanical characterization by compressive strength, tensile strength and elastic modulus [3]. Techniques such as optical microscopy and scanning electron microscopy, provide visual information, but with small depth of focus, being directed to surface analysis and fragmented samples by other experimental tests [4, 5]. On the other hand, non-destructive concrete testing techniques, such as ultrasound [6], electrical impedance tomography [7] and γ-ray or radiography inspection [8] can provide information on defects. Information on the different concrete composites is tough, especially due to the lack in the image spatial resolution and/or superposition of details. Neutron radiography/tomography [9] and X-ray computed tomography (CT) [5, 10, 11, 12, 13, 14, 15, 16, 17, 18, 19] may be able to identify the different concrete composites as well as its internal defects. Despite of its high concrete penetrability, the neutron inspection technique is not available in table top/portable equipment while the CT technique is available in a variety of forms.

CT has been applied as a useful tool in the microstructure analysis of sample model mortars [10, 11, 12, 13], sample model concretes [5, 14, 15, 16, 17] and real concrete specimen [18] without the need for any incursion and with the advantage of allowing to record images in two and three dimensions [19, 20]. X-ray CT can be implemented to investigate the failure process of concrete material under the coupledactions between sulfate attack and drying−wetting cycles [21]. For inspection of dams the whole structure is not accessible, even using ultra-high X-ray energies, provided by portable X-band Linac X-ray sources [18], which can often be used for the in-situ inspections of huge structures (such as bridges and other huge accessible structures). Therefore, for the inspection of the structure of the dam, a destructive technique based on local extraction of cylindrical concrete specimen, followed by radiography or computed tomography (CT) processing, needs to be carried out. It is worth noticing that, as already raised out by numerous citations in this section, there are a variety of tomography/microtomography works concerning the studies on cementitious materials, mainly on mortars. When the works are carried out on concrete specimens, they are based on gravel or crushed stone (rock particle size) with tiny granulometry (usually called stone dust) i.e., they can be used only as

sample models [14, 15]. Unfortunately, these models do not reproduce a practical application where CT could be useful. Stone dusts are used for fabrication of concrete blocks and pavers for riding arenas. Therefore, since the sample thickness are too small, and, consequently, the average spectral energy can be lower, phase contrast and differential attenuation contrast can be clearly seen for a concrete sample with a diameter of 10 mm and a monochromatic synchrotron X-ray beam of 53 keV [14].

To reproduce the reality, concrete specimens need to be evaluated with thicknesses at minimum of $\sim$50 mm, in order to preserve the structural properties of concrete composite materials [17, 18]. Then, the problem arises especially for the very well compressed real (and real size) concrete specimens (e.g., dam compacted concrete specimens) which shows densities of the different composites very close, then reducing the image contrast. The basic problem is the sample thickness, which attenuates too much the low energy X-ray spectrum. To circumvent this problem one can try to use filters in order to shift the spectrum to higher energies and in order to have as much as possible a quasi-monochromatic X-ray beam in an energy bandwidth around the best energy to provide the better contrast.

The use of X-ray filters is very well emploied for medical purposes. Almost always Aluminum (Al) filters are employed in order to reduce the low energy spectrum effect in the X-ray imaging system [22, 23]. The improvement of the image contrast by the use of X-ray filters have also been explored by the dentistry comunity [24, 25, 26]. Thick Copper (Cu) filters are also required by the EN ISO 11699-1 standard (which supersedes EN 584-1:2006) [27] for classification of film systems for industrial radiography. Therefore, studies on the influence of the physical filters in the improvementof the X-ray image (contrast enhancement) of concrete especimen are scarse. A 0.6 mm thick Copper (Cu) filter for beam hardening artifacts reducing has been recently proposed [18].

In this work, the use of thick Cu filters (>5 mm) as a contrast agent in X-ray imaging to resolve the different structures of highly compressed composite materials (real dam compacted concrete specimens) is proposed and optimized, as function of the image contrast and within the limits of our conventional X-ray inspection equipment, for X-ray voltages of 140 kV and 200 kV.

2. Background

Mass-concrete is widely used in construction of dams especially to try to minimize the temperature related microcracking [28]. The hydroelectric dam *Derivação do Rio Jordão*, in Brazil is a gravity type dam. It has been built on the roller-compacted concrete (RCC) [29]. The RCC technique produces in the dam's concrete, different levels of compaction. As deeper is the concrete in the structure, more compact the

concrete is. In Fig. 1 it is shown three different concrete specimens removed from the hydroelectric dam *Derivação do Rio Jordão*, with three different compaction levels: *(i)* low, *(ii)* medium and *(iii)* high. The compaction makes the X-ray inspection on these samples a challenge due to the slightly differences on the X-ray attenuation among the different concrete composites. This will be detailed discussed in the following section. As already described in the previous section, to reproduce the reality, concrete specimens need to be evaluated with thicknesses $>= 50$ mm, in order to preserve the structural properties of concrete composite materials [17, 18]. The present samples are in the down dimension limit (diameter of 50 mm). If one wants to evaluate thicker samples, X-ray generators working at higher voltages will be demanded.

The X-ray attenuation in plain concrete is high and even higher in compacted specimens. Then, in order to get sufficient visibility in X-ray images in such a way that different agglomerate structures inside a concrete specimen can be visualized, higher voltages need to be applied. Usually for ~ 50 mm thick concrete specimens, an X-ray tube with Tungsten (W) target operating at tensions above 140 kV [16, 17, 18] is required. Our experimental setup (Fig. 2) is based on a homemade X-ray industrial inspection system which is mounted inside a radiological protection hutch and is composed by *(i)* rails (to adjust source to sample and sample to detector distances); *(ii)* a COMET MXR 11-225HP X-ray tube (W target with a focal spot of 0.4 mm) mounted on a cart *(iii)* for translation on the rails; *(iv)* a PerkinElmer XRD-1621 flat panel X-ray detector (16 bit, 2048 $\times$ 2048 pixels, 200 $\times$ 200 μm each) and; *(v)* a rotation stage for sample support in both, radiography and tomography setups. The rotation stage is also mounted on the top of a cart *(vi)* for translation on the rails.
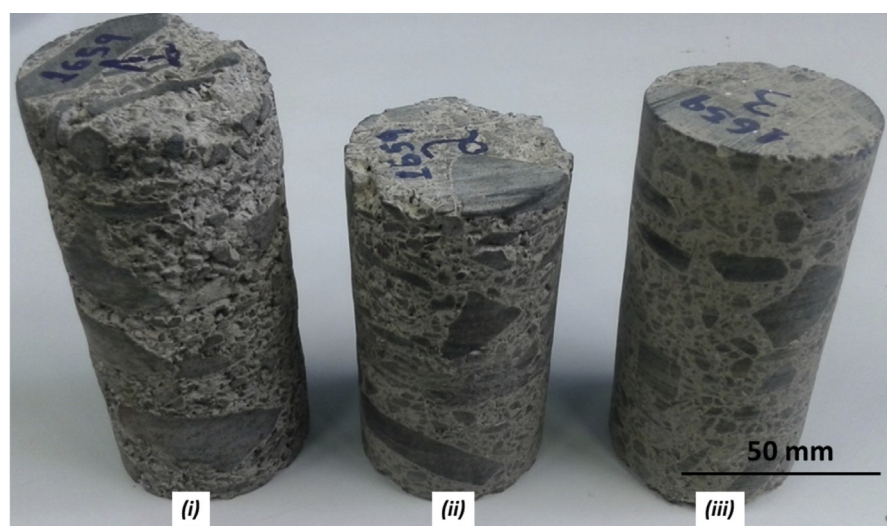

Fig. 1. Picture of the dam compacted concrete specimens with diameter of 50 mm: *(i)* Slightly compressed, *(ii)* medium compressed and *(iii)* highly compressed.
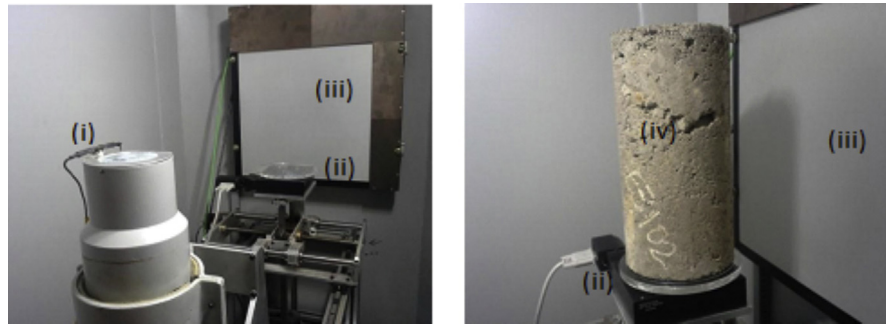
Fig. 2. Representation of the X-ray industrial inspection system *(i0* X-ray tube; *(ii)* a rotation stage for sample support in both radiography and tomography setups; (iii) flat panel X-ray detector; and *(iv)* concrete sample to be inspected.

In order to show the lack of visibility of different composites in X-ray images of dam compacted concrete specimens, projections (radiographies), for the three different samples under different compaction (Fig. 1) were acquired and are shown in Fig. 3 with its respective cross sections. The images were acquired using the broad X-ray spectrum provided by the W tube working at 200 kV without any filter (solid black line in Fig. 4). We also carried out images with the W tube working at 140 kV without any filter (solid green line in Fig. 4). However, since it was not possible to extract any better information in comparison with the images acquired at 200 kV, these results are not shown here. It is clear by the image cross sections (Fig. 3) that, even using 200 kV, the image contrast is huge, practically, 95%. This makes the visibility of different structures inside the compacted concrete specimen in an X-ray image a challenge. This occurs mainly because the low energy X-ray photons are hugely attenuated by the concrete. In order to increase the visibility, we propose to use a thick copper filter (Cu) in the W X-ray tube exit in order to take a hard X-ray spectrum with smaller chromaticity bandwidth. This will be discussed in the next section.

3. Theory

In order to improve the visibility in the X-ray images of different composites inside a compacted concrete specimen, we calculated the tungsten (W) X-ray tube emission spectra for tensions above 140 kV, by using TASMICS [30]. As mentioned in the previous section, in order to have a hard X-ray spectrum displaced to higher energies and with smaller spectral bandwidth, based on TASMICS calculations, we opted to use a Cu filter with an optimized thickness of 9.5 mm in tensions of 140 kV and 200 kV. Such optimization was made by calculating the different Al, Cu and Cu/Al filtered spectra (for different material thicknesses) with TASMICS, within the limits of our conventional X-ray inspection equipment, including the X-ray generator voltage (maximum of 225 kV). Then, with the different spectra, we simulated a
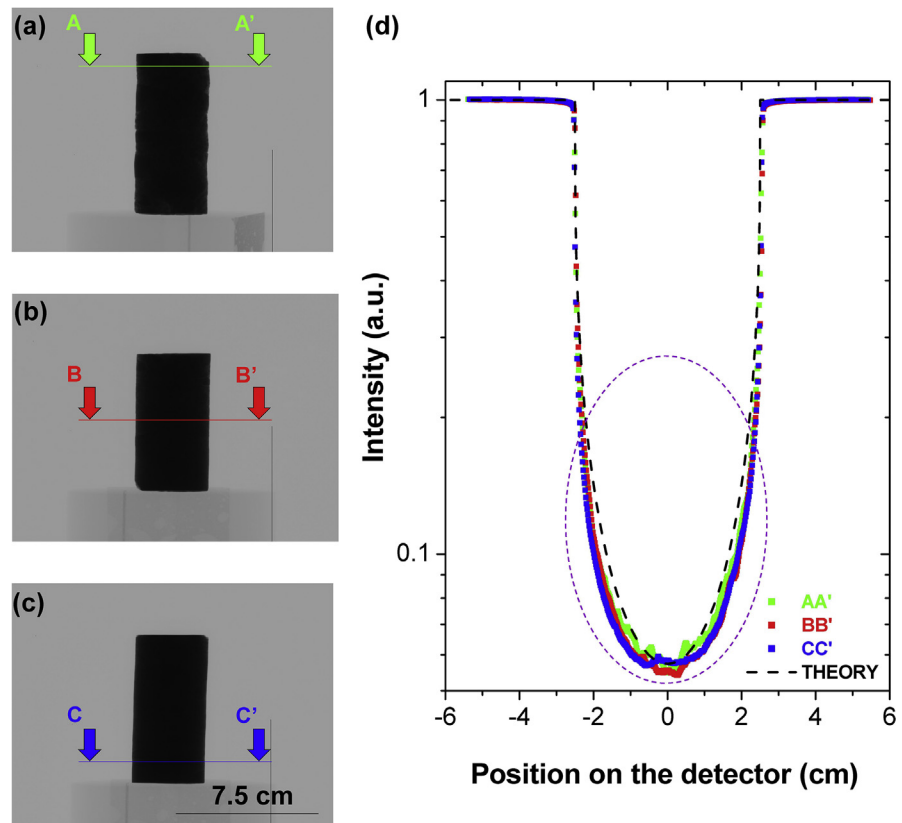
Fig. 3. (a−c) Radiographies acquired with Tungsten (W) X-ray tube (200 kV, 1 mA and exposure time of 1 s) without the use of filters. The unique filtration is the air (1.2 m) and the 0.8 mm thick (Be) window of the X-ray tube. (a) Slightly compressed, (b) medium compressed and (c) highly compressed. (d) Image cross sections taken at different depths on the concrete specimens (top AA'), middle (BB') and bottom (CC'). A theoretical image cross section based on a hypothetic homogeneous concrete sample is shown as black dashed line. Also, the purple dashed circle show the region of interest, where contrast is important in order to detect the different concrete composites. The vertical dark lines in the images are defective pixels.

theoretical image cross section based on a hypothetic homogeneous concrete sample with the same dimensions of our real sample. With these data, we selected the filtered spectra options those showed smaller attenuation in the central part of the sample. The calculated spectra are shown in Fig. 4 and the expected average energy values as well as the energy bandwidth is shown Table 1.

Also, in an attempt to quantitatively evaluate the image quality of the dam compacted concrete specimens, acquired at different image configurations, we bring to here different quantities defined by Pagot [31] and references therein. The area contrast (*C*) [Eq. (1)], the signal-to-noise ratio in the area case (*SNR_area*) [Eq. (2)], the visibility of the object edges (*V*) [Eq. (3)] and the signal-to-noise ratio for the edge case (*SNR_edge*) [Eq. (4)] are defined by:
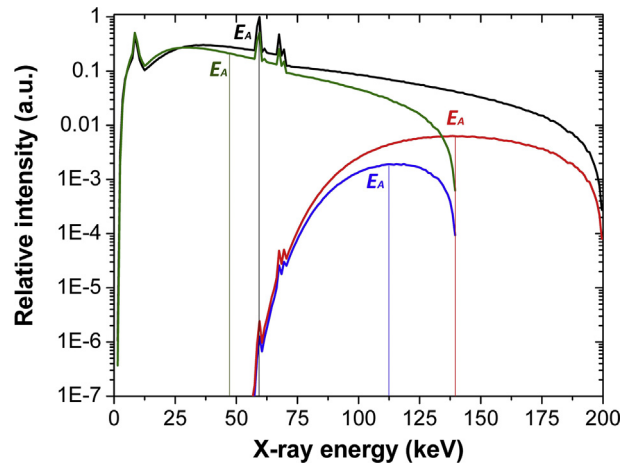
Fig. 4. Tungsten (W) X-ray tube emission spectra calculated by using TASMICS [14] for unfiltered 200 kV (solid black line), unfiltered 140 kV (solid green line), 200 kV with 9.5 mm thick Cu filter (solid red line) and 140 kV with 9.5 mm thick Cu filter (solid blue line). E_A, in different colors, means the average spectrum energy for each case.

$$C = \frac{\langle I_{spe}\rangle - \langle I_{backg}\rangle}{\langle I_{backg}\rangle} \tag{1}$$

$$SNR_{area} = \frac{\langle I_{spe}\rangle - \langle I_{backg}\rangle}{\sqrt{\sigma_{spe}^2 + \sigma_{backg}^2}} \tag{2}$$

$$V = \frac{I_{max} - I_{min}}{I_{max} + I_{min}} \tag{3}$$

$$SNR_{edge} = \frac{I_{max} - I_{min}}{\sqrt{2}\sigma_{backg}} \tag{4}$$

where $<I_{spe}>$ and $<I_{backg}>$ are the mean intensity values of a given area in the specimen and in the background, respectively; σ_{spe} and σ_{backg} are the standard deviations of the distributions of I_{spe} and I_{backg}; and, I_{max} and I_{min} are the maximum and minimum of the mean intensity profile across the specimen edge.

Table 1. Emission spectra properties for a W target X-ray tube under different voltages and filtration. Lα and Kα are the X-ray characteristic emission lines of W.

Voltage (kV)	Filter	Average Energy (keV)	Filtered Bandwidth (keV)
140	Cu − 9.5 mm	112	40
200	Cu − 9.5 mm	141	75
140	None	46 (WLα and WKα)	-
200	None	60 (WKα)	-

Eqs. (3) and (4) are focused on phase contrast X-ray imaging, for this reason they are focused on the specimen edges and this is not our purpose here. Thus, there is no need to deal with them. However, we defined two new quantities in order to better characterize our needs: the visibility inside the specimen (V_{ins}) [Eq. (5)] and the signal-to-noise ratio inside the specimen (SNR_{ins}) [Eq. (6)]. They are described as follows:

$$V_{ins} = \left| \frac{MAX(I_{ins} - I_{median\_ins}) - MIN(I_{ins} - I_{median\_ins})}{MAX(I_{ins} - I_{median\_ins}) + MIN(I_{ins} - I_{median\_ins})} \right| \tag{5}$$

$$SNR_{ins} = \left| \frac{MAX(I_{ins} - I_{median\_ins}) - MIN(I_{ins} - I_{median\_ins})}{\sqrt{2}.\sigma_{median\_ins}} \right| \tag{6}$$

where MAX and MIN are the maximum and minimum values of (I_{ins}-I_{median_ins}); I_{ins} is the intensity in each image pixel for the region inside the specimen; I_{median_ins} is the intensity in each image pixel for the regions inside the specimen, however filtered with a median filter with a k x k kernel. In other words, I_{median_ins} is the intensity registered in each image pixel inside a hypothetical homogeneous cilindrical concrete sample. Finally, σ_{median_ins} is the standard deviation of the distributions of I_{median_ins}.

4. Experimental

In order to test the X-ray imaging acquisition on the dam compacted concrete specimens with the Cu filter approach, the specimens, shown in Fig. 1, were imaged using a 9.5 mm thick Cu filter set just after the W X-ray tube exit. Images at two different voltages were acquired (140 kV and 200 kV). The resulting X-ray images, as well as their cross sections are shown in Figs. 5 and 6. To check the improvement in the visibility for the X-ray images of different composites inside the compacted concrete specimens, the parameters presented by the Eqs. (1), (2), (5), and (6) in the previous section were extracted from the image without the filter (Fig. 3) and from the images with filter (Figs. 5 and 6). A kernel of $k = 40$ was employed for the median filtered images. The results are presented in the Tables 2, 3, and 4.

It is worth noticing that the contrast (C) (which, as defined, show negative values) and the signal to noise ratio in the area case (SNR_{area}) are higher for the images acquired with the non-filtered spectrum (200 kV). This is expected since the low energies which have higher attenuation are contributing for these quantities. Also, in general, the higher is the dam concrete specimen compaction the higher is the value of C. For different compactions SNR_{area} was, approximately, constant for the images acquired with filtered spectra (at 200 kV and 140 kV). Since the contrasts (Cs) among the different concrete specimen compactions have a difference in the range of 16 %−30 %, this shows that care was taken during the exposure time of different
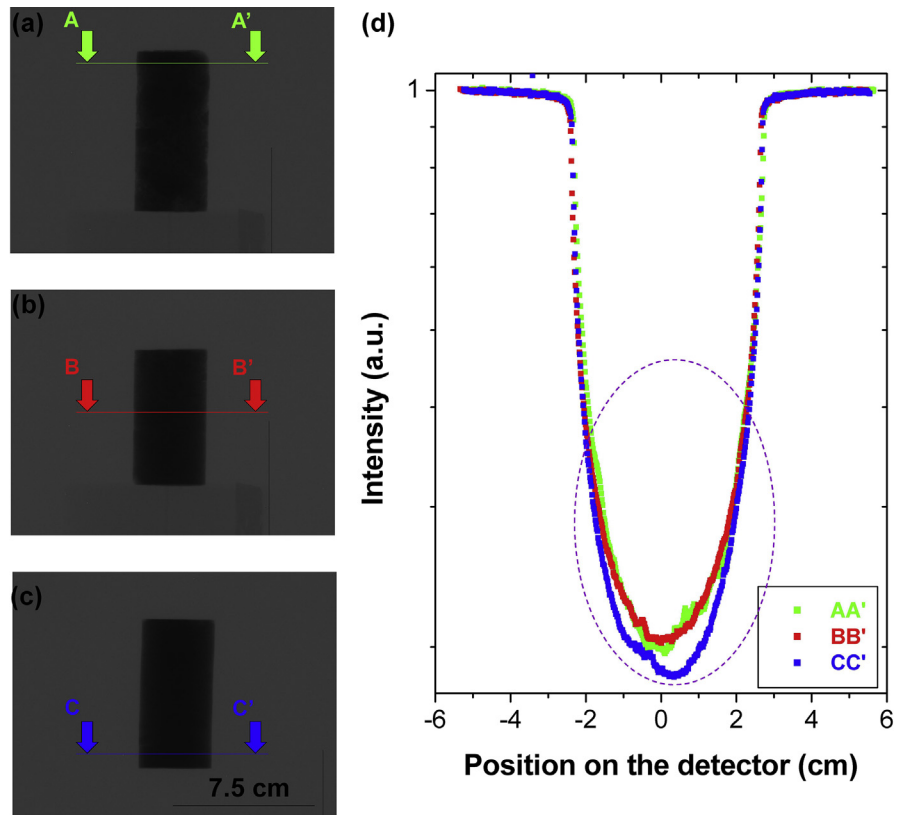
Fig. 5. (a−c) Radiographies acquired with Tungsten X-ray tube (140 kV, 3 mA and exposure time of 5 s) with the use of 9.5 mm thick Cu filter added to the air 1.2 m and the 0.8 mm thick Beryllium (Be) window of the X-ray tube. (a) Slightly compressed, (b) medium compressed and (c) highly compressed. (d) Image cross sections taken at different depths on the concrete specimens (top AA'), middle (BB') and bottom (CC') where, high contrast differences can be seen inside the purple dashed circle when compared with Fig. 3(d), showing the thick Cu filter capability in enhancing the contrast. The vertical dark lines in the images are defective pixels.

specimens at different spectra condition to assure the same statistics (e.g., for a filtered spectrum at lower voltages, higher exposure times were employed to assure the same statistics at higher voltages).

In terms of the visibility inside the object (V_{ins}) and signal do noise ratio inside the sample (SNR_{ins}) it is clear that the best option is the filtered spectra for any compaction of the concrete specimen. For the filtered 140 kV spectrum the visibility was higher, whereas in the filtered 200 kV spectrum the SNR_{ins} was higher. Both are expected since the former has a softer spectrum, however more monochromatic. Then, the specimen edges (while show less attenuation to the soft spectra) contribute to higher values of V_{ins}, while the center of the specimen contributes to have a lower SNR_{ins} because of the low intensity. The opposite analysis is true for the filtered 200 kV spectrum. One way to try to catch good V_{ins} and SNR_{ins} for both filtered
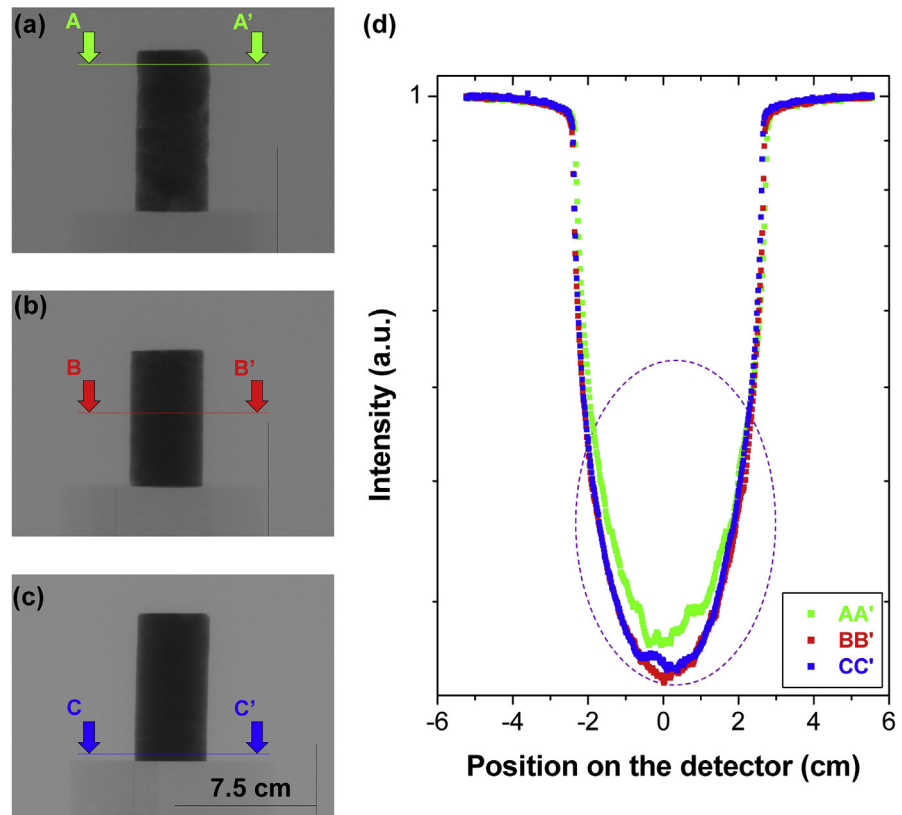
Fig. 6. (a–c) Radiographies acquired with Tungsten (W) X-ray tube (200 kV and 1 mA and exposure time of 6 s) with the use of 9.5 mm thick Cu filter added to the air (1.2 m) and to the 0.8 mm thick Beryllium (Be) window of the X-ray tube. (a) Slightly compressed, (b) medium compressed and (c) highly compressed. (d) Image cross sections taken at different depths on the concrete specimens (top AA'), middle (BB') and bottom (CC') where, high contrast differences can be seen inside the purple dashed circle when compared with Fig. 3(d), showing the thick Cu filter capability in enhancing the contrast. The vertical dark lines in the images are defective pixels.

spectra case would be to build bow-tie or through [22, 23] Cu filters in order to equalize the large image dynamical range of the concrete cylindrical samples.

For the non-filtered spectrum, V_{ins} and SNR_{ins} showed, approximately, the same values for all the compaction cases of the concrete specimens. This is a result of

Table 2. Parameters for image quality quantification defined by equations (1), (2), (3), (4), (5), (6) and extracted from the X-ray images shown in Figs. 3, 5, and 6 for the dam compacted concrete specimen *(i)* (Fig. 1).

Voltage (kV)	Filter	C	SNR_{area}	V_{ins}	SNR_{ins}
140	Cu − 9.5 mm	-0.19	-10.9	14.3	3.7
200	Cu − 9.5 mm	-0.27	-10.3	2.7	9.4
200	None	-0.06	-33.04	3.0	4.3

Table 3. Parameters for image quality quantification defined by equations (1), (2), (3), (4), (5), (6) and extracted from the X-ray images shown in Figs. 3, 5, and 6 for the dam compacted concrete specimen *(ii)* (Fig. 1).

Voltage (kV)	Filter	C	SNR_{area}	V_{ins}	SNR_{ins}
140	Cu − 9.5 mm	-0.21	-9.3	11.9	3.9
200	Cu − 9.5 mm	-0.25	-9.3	1.4	14.9
200	None	-0.05	-29.12	2.3	4.3

Table 4. Parameters for image quality quantification defined by equations (1), (2), (3), (4), (5), (6) and extracted from the X-ray images shown in Figs. 3, 5, and 6 for the dam compacted concrete specimen *(iii)* (Fig. 1).

Voltage (kV)	Filter	C	SNR_{area}	V_{ins}	SNR_{ins}
140	Cu − 9.5 mm	-0.18	-12.1	3.5	3.3
200	Cu − 9.5 mm	-0.25	-9.5	1.9	3.5
200	None	-0.04	-41.7	2.4	4.9

strong X-ray attenuation for all the specimens by the soft part of the non-filtered X-ray spectrum.

In order to further explore the statements above, X-ray computed tomography inspection was also carried out on the three dam compacted concrete specimens with the same equipment described in section 2 and schematically shown in Fig. 2. Tomography scans were carried out for the three different configurations: *(i)* W X-ray tube operating at 140 kV with 9.5 mm thick Cu filter; *(ii)* W X-ray tube operating at 200 kV with 9.5 mm thick Cu filter and; *(iii)* W X-ray tube operating at 200 kV without filter. For each concrete specimen, projections were acquired in the angular range from 0 to 360° in steps of one degree each (360 projections in total). The number of projections, in theory, is enough to do not degrade the voxel size, since it is more than half the number of pixels in the detected region of interest. Since we had three different concrete specimens to be imaged in three different configurations we carried out 9 tomography scans in total. The exposure times per projection ranged from 1 to 6 s, depending on the configuration. The source to sample distance were 1200 mm.

The tomography reconstruction results [two dimensional (2D) slices, based on filtered back-projection algorithm] on the three different dam compacted concrete specimens are shown, for the different image configurations, in Figs. 7, 8, and 9. The 2D slices were extracted from the same region, on the concrete specimens, where the cross sections, shown in Figs. 3, 5, and 6, were acquired.
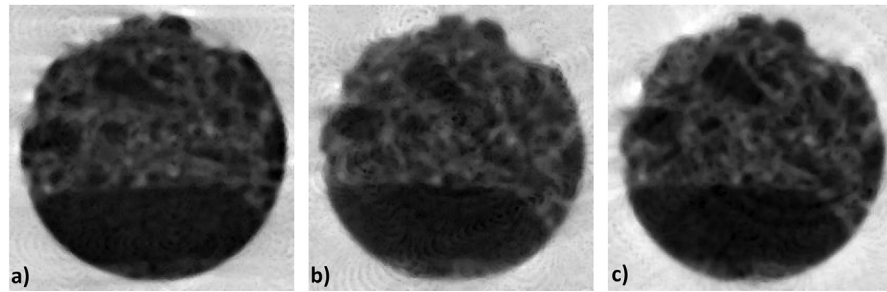
Fig. 7. Two dimensional (2D) tomography slices for the dam compacted concrete specimen *(i)* (Fig. 1). (a) 200 kV without filter, (b) 200 kV with 9.5 mm thick Cu filter and, (c) 140 kV with 9.5 mm thick Cu filter. Gravel can be identified by the darker structures.

Fig. 8. Two dimensional (2D) tomography slices for the dam compacted concrete specimen *(ii)* (Fig. 1). (a) 200 kV without filter, (b) 200 kV with 9.5 mm thick Cu filter and, (c) 140 kV with 9.5 mm thick Cu filter. Gravel can be identified by the darker structures.
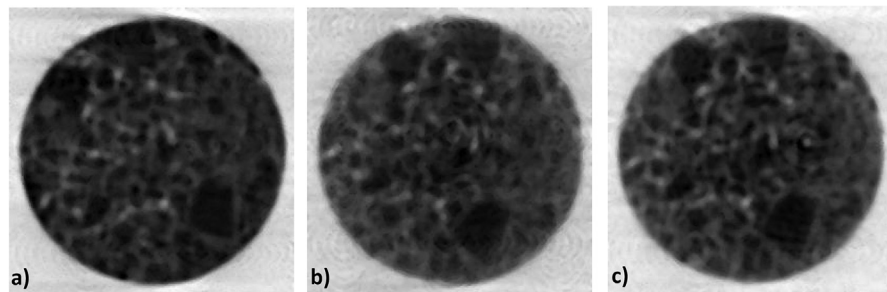
A similar quantitative analysis, made for the radiography results, was carried out for the tomography slices. However, since different mathematical filters were applied into the tomography reconstruction, we modified Eqs. (5) and (6) to Eqs. (7) and (8), as follows:
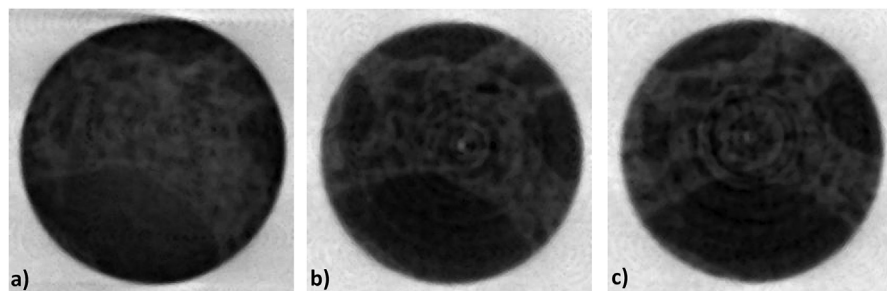

Fig. 9. Two dimensional (2D) tomography slices for the dam compacted concrete specimen *(iii)* (Fig. 1). (a) 200 kV without filter, (b) 200 kV with 9.5 mm thick Cu filter and, (c) 140 kV with 9.5 mm thick Cu filter. Gravel can be identified by the darker structures. Even applying some mathematical filters for ring artifacts removing, some of them are still present in the tomography slices. This is due to the low dynamical range in the image within the strong attenuation region of the highly compressed sample.

Table 5. Parameters for the 2D tomography quality quantification defined by equations (7), (8) and extracted from the images shown in Fig. 7 for the dam compacted concrete specimen *(i)* (Fig. 1).

Voltage (kV)	Filter	V_{ins}	SNR_{ins}
140	Cu − 9.5 mm	0.31	5.2
200	Cu − 9.5 mm	0.28	4.1
200	None	0.22	4.9

Table 6. Parameters for the 2D tomography quality quantification defined by equations (7), (8) and extracted from the images shown in Fig. 7 for the dam compacted concrete specimen *(ii)* (Fig. 1).

Voltage (kV)	Filter	V_{ins}	SNR_{ins}
140	Cu − 9.5 mm	0.46	5.9
200	Cu − 9.5 mm	0.53	6.0
200	None	0.22	7.6

Table 7. Parameters for the 2D tomography quality quantification defined by equations (7), (8) and extracted from the images shown in Fig. 7 for the dam compacted concrete specimen *(iii)* (Fig. 1).

Voltage (kV)	Filter	V_{ins}	SNR_{ins}
140	Cu − 9.5 mm	0.40	6.0
200	Cu − 9.5 mm	0.47	6.1
200	None	0.18	6.9

$$V_{ins\_slice} = \left| \frac{MAX(I_{ins\_slice}) - MIN(I_{ins\_slice})}{MAX(I_{ins\_slice}) + MIN(I_{ins\_slice})} \right| \qquad (7)$$

$$SNR_{ins\_slice} = \left| \frac{MAX(I_{ins\_slice}) - MIN(I_{ins\_slice})}{\sqrt{2} . \sigma_{ins\_slice}} \right| \qquad (8)$$

where, now, *MAX* and *MIN* are the maximum and minimum values of (I_{ins_slice}); I_{ins_slice} is the intensity in each image pixel for the region inside the specimen slice and σ_{ins_slice} is the standard deviation of I_{ins_slice}. The analyses taken on the 2D tomography images shown in Figs. 7, 8, and 9, based on Eqs. (7) and (8), are presented in the Tables 5, 6, and 7. In terms of the visibility inside the slice (V_{ins_slice}) and signal to noise ratio inside the slice (SNR_{ins_slice}), it is clear that the best option are the filtered spectra for any compaction of the concrete specimen. For the filtered 140 kV spectrum the visibility was higher, only

for the specimen *(i)* which is less compacted. For the more compacted specimens the use of 9.5 mm thick Cu filtered 200 kV spectrum showed the best image visibility. The SNR_{ins_slice} was lower for all filtered images, having, approximately the same values for 140 kV and 200 kV. This means that our strategy of using a thick Cu filter is efficient. Based on the visibility results the best choice for tomography purposes is the use of the 9.5 mm thick Cu filtered 200 kV spectrum.

5. Conclusion

Dam concrete specimens are difficult to be investigated with conventional X-ray inspection equipment due to its high compaction. However, we have shown here optimized parameters (by choosing the filter material and its proper thickness) for improving image quality on the radiography and tomography inspection of real (and real size) dam compacted concrete specimens. Within the limits of our conventional X-ray inspection equipment, by applying a tension of 200 kV with a 9.5 mm thick Cu filter, we were able to distinguish the gravel from the other agglomerate composites in compacted concrete specimens. Cement and sand grains as well as porosity were not detected mainly due to the low spatial resolution of our detector system. Better results on real size specimens can be further improved if one uses the now available high voltage microfocus X-ray tubes ($>=$ 200 kV) as well as better resolution flat-panel detectors in such a way we can explore phase contrast and filtered X-ray spectrum. Also, the use of bow-tie (or, through) Cu filters are envisaged in order to equalize the large image dynamical range of the concrete cylindrical samples. At last, as mentioned within the manuscript text, to reproduce the reality, concrete specimens need to be evaluated with thicknesses $>=$ 50 mm. The samples inspected here are in the down dimension limit. Then, if one wants to evaluate thicker samples, X-ray generators working at higher voltages will be demanded.

Declarations

Author contribution statement

Walmor Godoi: Conceived and designed the experiments; Performed the experiments; Analyzed and interpreted the data; Contributed reagents, materials, analysis tools or data; Wrote the paper.

Giovanna Coraiola, Sebastiao Ribeiro Junior, Vitoldo Swinka-Filho, Klaus de Geus, Kleber Portella, Betina Medeiros, Fabricio Andrade, Marcelo Honnicke: Conceived and designed the experiments; Performed the experiments; Analyzed and interpreted the data.

Funding statement

Competing interest statement

The authors declare no conflict of interest.

Additional information

No additional information is available for this paper.

References

[1] J.C.A. Galvão, K.F. Portella, A. Joukoski, R. Mendes, E.S. Ferreira, Use of waste polymers in concrete for repair of dam hydraulic surfaces, Constr. Build. Mater. 25 (2011) 1049–1055.

[2] P.K. Mehta, P.J.M. Monteiro, Concrete: Microstructure, Properties and Materials, fourth ed., McGraw-Hill Education, 2014.

[3] A.M. Neville, Properties of Concrete, fourth ed., John Wiley & Sons, Inc., New York, 1996.

[4] B. Georgali, P.E. Tsakiridis, Microstructure of fire-damaged concrete. A case study, Cement Concr. Compos. 27 (2005) 255–259.

[5] D. Fukuda, M. Maruyama, Y. Nara, D. Hayashi, H. Ogawa, K. Kaneko, Observation of fracture sealing in high-strength and ultra-low-permeability concrete by micro-focus X-ray CT and SEM/EDX, Int. J. Fract. 188 (2014) 159–171.

[6] Yu E. Kornilovich, Ultrasound in the Production and Inspection of Concrete, first ed., Springer, 1965.

[7] K. Karhunen, A. Seppanen, A. Lehikoinen, P.J. M.Monteiro J.P. Kaipio, Electrical resistance tomography imaging of concrete, Cement Concr. Res. 40 (2010) 137–145.

[8] V.M. Malhotra, N.J. Carino, Handbook on Nondestructive Testing of Concrete, second ed., CRC Press LLC, Boca Raton, 2004.

[9] K. Van Tittelboom, D. Snoeck, P. Vontobel, F.H. Wittmann, N. De Belie, Use of neutron radiography and tomography to visualize the autonomous crack

sealing efficiency in cementitious materials, Mater. Struct. 46 (2013) 105−121.

[10] I. Tekin, R. Birgul, I.O. Yaman, O. Gencel, H.Y. Aruntas, Monitoring macro voids in mortars by computerized tomography method, Measurement 63 (2015) 299−308.

[11] E. Landis, E. Nagy, D. Keane, Microstructure and fracture in three dimensions, Eng. Fract. Mech. 70 (2003) 911−925.

[12] N. Burlion, D. Bernard, D. Chen, X-ray microtomography: Application to microstructure analysis of a cementitious material during leaching process, Cement Concr. Res. 36 (2006) 346−357.

[13] M.A.B. Promentilla, T. Sugiyama, X-ray microtomography of mortars exposed to freezing-thawing action, J. Adv. Concrete Technol. 8 (2010) 97−111.

[14] A. Saparata, M. Ruiz-Yaniz, I. Zanette, A. Rack, F. Pfeiffer, J. Herzen, Multi-contrast 3D X-ray imaging of porous and composite materials, Appl. Phys. Lett. 106 (2015) 154102.

[15] S. Lu, E.N. Landis, D.T. Keane, X-ray microtomographic studies of pore structure and permeability in Portland cement concrete, Mater. Struct. 39 (2006) 611−620.

[16] L. Skarzynski, J. Tejchman, Experimental investigations of fracture process in concrete by means of X-ray micro-computed tomography, Strain 52 (2016) 26−45.

[17] A. du Plessis, B.J. Olawuyi, W.P. Boshoff, S.G. le Roux, Simple and fast porosity analysis of concrete using X-ray computed tomography, Mater. Struct. 49 (2016) 553−562.

[18] M. Ueaska, K. Dobashi, T. Fujiwara, C. Pei, W. Wu, J. Kusano, N. Nakamura, M. Yamamoto, E. Tanabe, S. Ohya, Y. Hattori, I. Miura, H. Honma, M. Ishida, Y. Kimura, On-site nondestructive inspection by upgraded portable 950 keV/3.95 MeV X-band linac x-ray sources, J. Phys. B At. Mol. Opt. Phys. 47 (2014) 234008.

[19] W.C. Godoi, K. de Geus, V. Swinka-Filho, R.R. da Silva, Volume and surface measurements of flaws in polymeric insulators using X-ray computed tomography, Insight 50 (2008) 554−559.

[20] R. Mendes, K.F. Portella, W.C. Godoi, J.C.A. Galvão, A. Joukoski, P. Martins, V. Swinka-Filho, K. K de Geus, J.C.A. Galvão, Determination

of crushed stone volume in concrete cores from hydroelectric power plant dams by three-dimensional tomography, Insight 51 (2009) 654−659.

[21] J. Yuan, Y. Liu, Z. Tan, B. Zhang, Investigating the failure process of concrete under the coupled actions between sulfate attack and drying−wetting cycles by using X-ray CT, Constr. Build. Mater. 108 (2016) 129−138.

[22] T.S. Curry, J.E. Dowdey, R.E. Murry, Christensen's Physics of Diagnostic Radiology, fourth ed., Lippincott Williams & Wilkins, Philadelphia, 1990.

[23] S.C. Bushong, Radiologic Science for Technologists, Mosby Elsevier 9th Edition, St. Louis, 2008.

[24] J. Stecke, A.D. Cruz, S.M. Almeida, F.N. Bóscolo, Alternative X-ray filters for an intra-oral digital radiographic system, Dentomaxillofacial Radiol. 41 (2012) 361−366.

[25] M.L. Kohn, A.W. Gooch, W.S. Keller, Filters for radiation reduction: a comparison, Radiology 167 (1988) 255−257.

[26] S.M. Mariello, D.B. Washburn, S.R. Matteson, Effects of rare-earth filters on patient exposure and image contrast, J. Dent. Res. 66 (1987) 1326−1330.

[27] EN ISO 11699-1, 2011 Non-Destructive Testing − Industrial Radiographic Film − Part 1 : Classification of Film Systems for Industrial Radiography, European Committee for Standardization (CEN), 2011.

[28] E.J.V. Vicencio-Camacho, Analysis of Microcrack Behavior in Mass concrete, MsC. Thesis, University of Florida, 2006.

[29] L. Donghai, Z.-L. Li, J.L. Liu, Experimental study on real-time control of roller compacted concrete dam compaction quality using unit compaction energy indices, Constr. Build. Mater. 96 (2015) 567−575.

[30] A.M. Hernandez, J.M. Boone, Tungsten anode spectral model using interpolating cubic splines: unfiltered x-ray spectra from 20 kV to 640 kV, Med. Phys. 41 (2014), 042101.

[31] E. Pagot, S. Fiedler, P. Cloetens, A. Bravin, P. Coan, K. Fezzaa, J. Baruchel, J. Härtwig, Quantitative comparison between two phase contrast techniques: diffraction enhanced imaging and phase propagation imaging, Phys. Med. Biol. 50 (2005) 709−724.